J. Fluid Mech. (2024), *vol*. 994, A1, doi:10.1017/jfm.2024.562

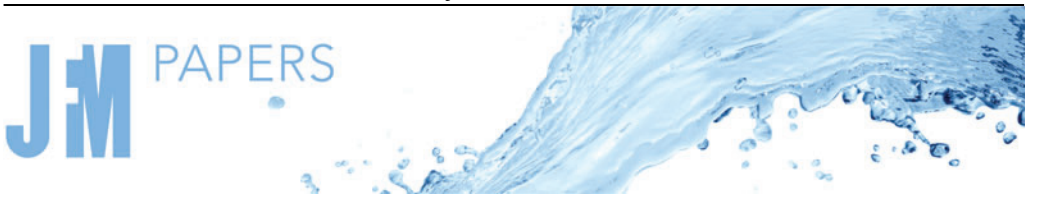

Drag coefficient for irregularly shaped grains: rotational dependence at various Reynolds numbers

Álvaro Vergara[1], **Deheng Wei**[1,2,3,†] **and Raúl Fuentes**[1]

[1]Institute of Geomechanics and Underground Technology, Faculty of Civil Engineering, RWTH Aachen University, 52074 Aachen, Germany

[2]Key Laboratory of Ministry of Education on Safe Mining of Deep Mines, School of Resources and Civil Engineering, Northeastern University, Shenyang 110819, PR China

[3]School of Civil Engineering, The University of Sydney, NSW 2006, Australia

(Received 23 January 2024; revised 6 June 2024; accepted 6 June 2024)

The nature and behaviour of the drag coefficient C_D of irregularly shaped grains within a wide range of Reynolds numbers Re is discussed. The morphology of the grains is controlled by their fractal description, and they differ in shape. Using computational fluid dynamics tools, the characteristics of the boundary layer at high Re has been determined by applying the Reynolds-averaged Navier–Stokes turbulence model. Both grid resolution and mesh size dependence are validated with well-reported previous experimental results applied in flow around isolated smooth spheres. The drag coefficient for irregularly shaped grains is shown to be higher than that for spherical shapes, also showing a strong drop in its value at high Re. This drag crisis is reported at lower Re compared to the smooth sphere, but higher critical C_D, demonstrating that the morphology of the particle accelerates this crisis. Furthermore, the dependence of C_D on Re in this type of geometry can be represented qualitatively by four defined zones: subcritical, critical, supercritical and transcritical. The orientational dependence for both particles with respect to the fluid flow is analysed, where our findings show an interesting oscillatory behaviour of C_D as a function of the angle of incidence, fitting the results to a sine-squared interpolation, predicted for particles within the Stokes laminar regime ($Re \ll 1$) and for elongated/flattened spheroids up to $Re = 2000$. A statistical analysis shows that this system satisfies a Weibullian behaviour of the drag coefficient when random azimuthal and polar rotation angles are considered.

Key words: porous media, fractals

† Email addresses for correspondence: wei@gut.rwth-aachen.de, dwei3017@uni.sydney.edu.au

1. Introduction

A variety of physical phenomena in nature involve the dynamics of particles immersed in fluid media. Geosciences, astrophysics, the chemical industry, mineral treatment and material sciences are some of the disciplines that encompass the study of the interactions of discrete systems with fluid flow. Segregation of granular matter, asteroid penetration into the atmosphere, sediment transport in natural systems, handling of mineral grains in the mining industry, are some engineering applications where this is particularly relevant. This type of system is usually studied from a hydrodynamic perspective using the forces acting on the surface of the body. This involves analysing the drag coefficient $C_D = 2\,|\boldsymbol{F}_D|/(\rho_f\,|\boldsymbol{u}_\infty|^2\,A_p)$ as a dimensionless quantity capable of describing the resistance force exerted by the body within a fluid medium, where $\boldsymbol{F}_D$ is the drag force exerted on the body, ρ_f is the density of the fluid, $\boldsymbol{u}_\infty$ is the terminal or free-stream velocity of the fluid, and A_p is the projected area of the body on a plane normal to the direction of the fluid flow.

The importance of the drag coefficient lies in the optimisation and understanding of the fluid dynamics or the rheological behaviour of solid bodies within a fluid medium. Its engineering applications extend to aerodynamic design of vehicles (Bayındırlı & Çelik 2018), net design in aquaculture and oceanography (Tsukrov *et al.* 2011), optimisation of pneumatic transport in the food industry (Defraeye, Verboven & Nicolai 2013), and hydrodynamic behaviour of plant layers (Etminan, Lowe & Ghisalberti 2017), among others. Oggiano *et al.* (2004) performed an interesting application of drag in the aerodynamic behaviour of athletes, determining the influence of surface roughness on resistance at high Reynolds numbers, and how these results extrapolate to drag on rough cylinders.

Nevertheless, the dynamics of the external flow has been analysed from fundamental geometries from both analytical and experimental perspectives. Pioneering studies have determined the influence of drag on spherical bodies (Achenbach 1972; Haider 1989; Constantinescu & Squires 2004; Sun *et al.* 2005) as a basis for extending it to more complex geometries, as ellipsoids (Ouchene *et al.* 2015; Sanjeevi & Padding 2017; Sanjeevi, Kuipers & Padding 2018), spherical clusters (Tran-Cong, Gay & Michaelides 2004), cylinders (Lam & Lin 2009; Cadot *et al.* 2015), agglomerates (Chen, Chen & Fu 2022) and granular media (Guillard, Forterre & Pouliquen 2014; Jing *et al.* 2022).

In general, the drag coefficient depends on the Reynolds number Re, especially for $Re < 10^4$; above this value, the drag coefficient remains practically constant due to the transition to turbulence. Additionally, for smooth bodies (such as spheres and cylinders) in highly turbulent flows, there is also a drag crisis, where the drag coefficient decreases drastically up to a critical value, beyond which it then increases gradually with increasing Re until reaching a relatively constant value. This drag crisis is related to the turbulent transition of the boundary layer when Re is relatively large. However, its existence and the behaviour during this transition have not been shown for irregularly shaped particles, despite initial evidence showing that.

This phenomenon has been of interest to understand the behaviour of the drag coefficient beyond smooth geometries. Beratlis, Balaras & Squires (2019) carried out a set of direct numerical simulations (DNS) to determine the origin of drag patterns around dimpled spheres at post-critical Re. They found that the dimples, although reducing the critical value of the Reynolds number relative to that of the smooth sphere, impose a local drag penalty, which contributes significantly to the overall drag force.

The effect of rotational dependence of smooth bodies on drag is described well by Sanjeevi & Padding (2017), who derived a periodic behaviour of the drag coefficient as

the ellipsoidal particle is rotated under the circumstance where its longest axis, shortest axis and flow directions are always on the same plane, for Re up to 2000. However, many questions about the influence of surface irregularity and the complete randomness of rotation on the fluid dynamic behaviour of the particle remain to be resolved, especially again under turbulent regimes.

Regarding the analysis of drag in irregularly shaped particles, the difficulty lies in the morphological description of the particle. Different shape factors have been described to encompass the geometry of irregular particles and base their analysis on these factors. Dioguardi, Mele & Dellino (2017) presented a model capable of describing the drag coefficient of irregularly shaped particles from the sphericity and circularity of the geometries, in a wide range of Re (0.03–10 000). Sommerfeld & Qadir (2018) used these shape factors and applied the lattice Boltzmann method with local grid refinement on non-spherical irregular geometries at Re up to 200, finding patterns similar to spherical bodies in both drag and lift. Some applications of drag on irregularly shaped particles have been analysed by Sun *et al.* (2018) and Wang *et al.* (2018).

The irregularity of the particle surface directly impacts the drag coefficient. Zhang *et al.* (2023) proposed various drag coefficient models for irregularly shaped particles for $Re \leq 200$. They determined that C_D increases as the particle surface becomes more irregular. They also showed that C_D varies slowly at low Reynolds numbers for different fluid incidence angles, while it does so more rapidly at high Re. However, they did not study the behaviour for very large Re.

Gai & Wachs (2023) explored the influence of the angularity of Platonic bodies on drag and lift coefficients. Their findings highlight that at low Reynolds numbers, the cross-sectional area of the particle has a high influence on the drag coefficient, while at high Reynolds numbers, the angular position of the particle with respect to the flow tends to have a greater influence.

Recently, Michaelides & Feng (2023) performed a complete review of the different models to estimate the drag coefficients for both symmetrical particles and irregularly shaped particles. In the review, they critically discuss the advantages and difficulties when using descriptors and shape factors in particle morphology, and its different applications and restrictions when evaluating these correlations in computational fluid dynamics (CFD) codes.

The objective of this study is to contribute to the characterisation of the fluid dynamic behaviour of irregularly shaped particles in a wide spectrum of flow regimes $Re = 1$–10^7, and unravel the rotational dependence effect on the drag coefficient. This paper is divided into the following sections. In § 2, we describe the CFD tools applied to resolve pressure and velocity fields, within the set-up geometry, both for model validation and for obtaining the drag forces for irregular geometries. The results of the drag and the rotational influence for the range of laminar and turbulent flow are presented in § 3, highlighting and discussing the different findings of the fluid dynamic behaviour of the drag for this type of geometry. The main conclusions of this research are summarised in § 4.

2. Methods

2.1. *Numerical resolution and geometric considerations*

The flow development is computed by solving numerically the Navier–Stokes equations for viscous, incompressible and isothermal flow:

$$\nabla \cdot \boldsymbol{u} = 0, \tag{2.1a}$$

$$\rho_f(\boldsymbol{u}\cdot\nabla)\boldsymbol{u} = \nabla\cdot[-pI + \mu_f(\nabla\boldsymbol{u} + (\nabla\boldsymbol{u})^{\mathrm{T}})], \tag{2.1b}$$

where $\boldsymbol{u}$ is the velocity field inside the fluid domain, ρ_f is the fluid density, μ_f is the fluid dynamic viscosity, and p is the pressure field in the system.

The flow regime at high *Re* is evaluated using the Reynolds-averaged Navier–Stokes (RANS) turbulence model applied to the transport equations for shear stress (k-ω) viscous model (Menter 1994). Although its capacity to resolve turbulent elements in the boundary at high Reynolds numbers has been investigated, some authors hold the view very good accuracy may not obtained by RANS-based CFD, and often the numerical solution is partly to blame for the errors. This latter problem will be solved by fine grid or mesh refinement in the fluid region, and increased computing power, although the convergence may be difficult (Roy *et al.* 2006). Compared with other advanced CFD methods, i.e. DNS and large-eddy simulations, the RANS model is computationally less expensive, facilitating the possibility of systematic study on rotation-angle-dependent drag coefficients of irregularly shaped grains under various Reynolds number in this study. Further, according to Yang *et al.* (2014), RANS simulation is good enough for capturing overall flow trends; however, if one is interested in getting reasonably accurate estimates of velocity magnitudes, flow structures, turbulence magnitudes and their distributions, then one must resort to other advanced CFD simulations. In this study, our focus is on the overall drag force on the grain rather than on comparing the flow structures induced by rotation angles. Validations from both numerical (DNS for the irregularly shaped grain) and experimental (the spherical grain) investigations for our RANS results will be given in the following sections.

The numerical resolution is obtained from the pressure–velocity coupled scheme (based on pressure), which allows the simultaneous resolution of the equations of motion and continuity, ensuring greater robustness of the numerical solution. The spatial discretisation follows a second-order method, given the irregular flow conditions in the boundary layer, especially in the turbulent regime at extremely high *Re*.

The irregular geometries of the grains were created from a practical method for generating irregularly shaped particles using a fractal dimension as a descriptor parameter of the grain morphology. It uses spherical harmonics that allow us to define and control the morphology of the particle from its fractal properties – its shape, roundness and texture – based on the model presented by Wei *et al.* (2018). The generated irregularly shaped particles used in this paper are shown in figures 1(*a*,*b*).

The particles are characterised by their axial asymmetry caused by the presence of dimples and ridges distributed randomly over their entire surface. The fractal dimension D_f is 2.287 and 2.420 for the two grains, typically frequent for Leighton Buzzard sand (LBS) in Bedfordshire, and highly decomposed granite (HDG), respectively. Those values are based on the statistical relationship between the spherical harmonic descriptor and the spherical harmonic degree. The characteristic lengths in the longest, intermediate and shortest dimensions of a box containing the particle inside are 2.87 mm, 2.49 mm and 2.05 mm for LBS, and 5.12 mm, 3.02 mm and 2.96 mm for HDG grain. Table 1 summarises the main shape descriptors for both particles; the definitions are based on those presented by Angelidakis *et al.* (2022) and Michaelides & Feng (2023).

We define the Reynolds number based on the projected area-equivalent particle diameter d_p as $Re = \rho_f\,|\boldsymbol{u}_\infty|\,d_p/\mu_f$. The equivalent diameter of the irregularly shaped particle is obtained from the diameter of a circumference with the same equivalent projected area of the particle, A_p, on the plane perpendicular to the fluid flow, $d_p = \sqrt{4A_p/\pi}$.

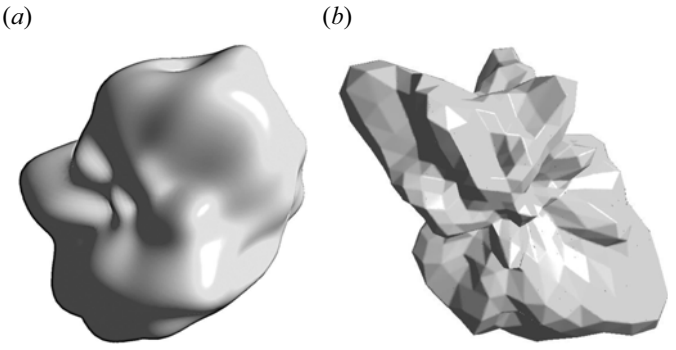

Figure 1. Geometry of irregularly shaped particles used in the study of the drag coefficient. (*a*) Grain with fractal dimension $D_f = 2.287$, typically frequent for Leighton Buzzard sand. (*b*) Grain with fractal dimension $D_f = 2.420$, frequent for highly decomposed granite.

	Flatness	Elongation	Compactness	Sphericity	D_f
Leighton Buzzard sand	0.830	0.861	0.835	0.835	2.287
Highly decomposed granite	0.980	0.590	0.733	0.656	2.420

Table 1. Particle shape descriptors of Leighton Buzzard sand and highly decomposed granite, based on the definitions presented in Angelidakis, Nadimi & Utili (2022) and Michaelides & Feng (2023). The flatness is herein defined as the ratio between the lengths of the major and intermediate axes; the elongation is defined as the ratio between the lengths of the intermediate and minor axes; the compactness is defined as the ratio of the area of the particle to the square of its maximum perimeter; and the sphericity is defined as the ratio of the surface area of the sphere with equivalent volume to the actual surface area of the particle.

2.2. *Numerical set-up and grid resolution influence*

The configuration applied in the simulations emulates those developed in physical experimentation, with a solid body inside a wind tunnel through which the fluid flows and where the resulting forces on the surface of the body under study are analysed. Figure 2(*a*) shows the computational domain used in all the simulations. These dimensions were chosen to avoid any influence of the geometry walls.

We adopt the boundary conditions considering the inlet flow at free-stream velocity by setting $u_x = u_{inlet}$ and $u_y = u_z = 0$, which are also for a no-slip condition in the walls. A pressure outlet past the irregularly shaped grain is given by setting $p = 0$ and $\mathrm{d}u_x/\mathrm{d}x = \mathrm{d}u_y/\mathrm{d}x = \mathrm{d}u_z/\mathrm{d}x = 0$, while $u_x = u_y = u_z = 0$ is set in the fluid–solid interface.

To determine the resolution of the modelling grid, the calibration is performed by running 27 simulations, and using an isolated smooth sphere and comparing its drag coefficient as a function of Reynolds number with the experimental values obtained by Achenbach (1972). Critically, we concentrate on the size of the mesh around the particle in order to capture the boundary layer effects even at high Reynolds numbers. Figure 2(*b*) shows the meshing detail in the zone close to the boundary layer, where the thick black line represents the refinement required to capture the information at the boundary between the irregularly shaped grain and the fluid (smaller mesh elements).

The analysis of the rotational dependence of the drag coefficient is performed considering two types of particle rotation respect to the fluid flow: azimuthal rotation α (anticlockwise with respect to the z-axis on the meridional x–y plane), and polar rotation β (anticlockwise with respect to the y-axis on the x–z plane) as shown in figures 2(*c*,*d*).

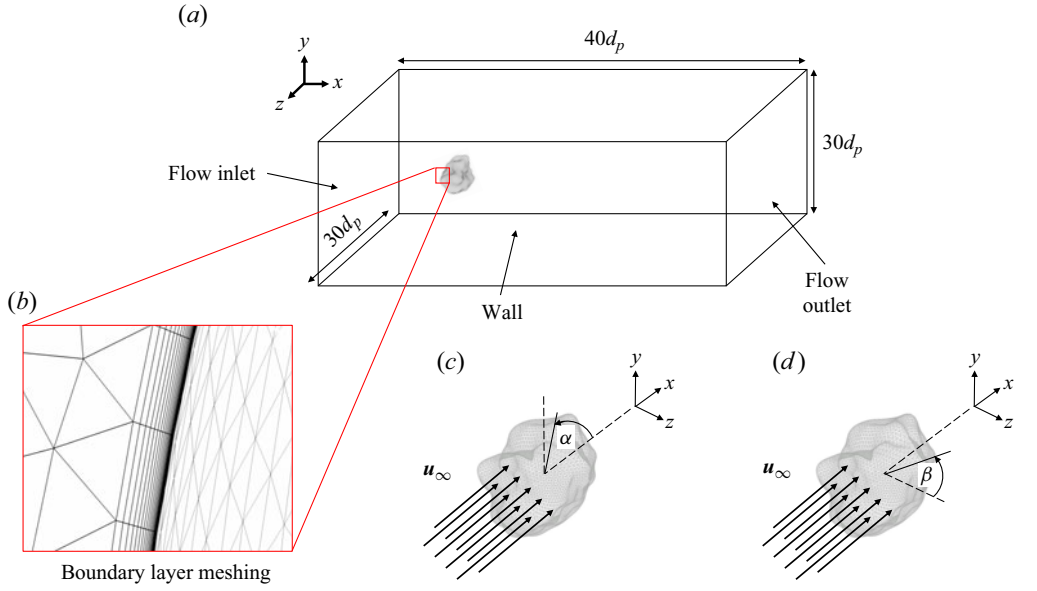

Figure 2. (*a*) Computational domain used in the numerical study, whose dimensions make it possible to avoid the influence of the fluid–wall interaction on the fluid–particle interaction (not to scale). (*b*) Unstructured mesh applied in conjunction with inflation methods to optimise turbulence capture in the boundary layer. (*c*) Azimuthal rotation α anticlockwise with respect to the z-axis (x–y meridional plane). (*d*) Polar rotation β anticlockwise with respect to the y-axis (x–z meridional plane).

Formally, let $[x_0 \quad y_0 \quad z_0]^{\mathrm{T}}$ be the original coordinates of the points on the surface of the particle, and the updated coordinates of said points, $[x_u \quad y_u \quad z_u]^{\mathrm{T}}$, once the particle is rotated, are given by

$$\begin{bmatrix} x_u \\ y_u \\ z_u \end{bmatrix} = \begin{bmatrix} \cos\beta & 0 & -\sin\beta \\ 0 & 1 & 0 \\ \sin\beta & 0 & \cos\beta \end{bmatrix} \times \begin{bmatrix} \cos\alpha & \sin\alpha & 0 \\ -\sin\alpha & \cos\alpha & 0 \\ 0 & 0 & 1 \end{bmatrix} \times \begin{bmatrix} x_0 \\ y_0 \\ z_0 \end{bmatrix}. \tag{2.2}$$

For the first analysis, the complete rotation of the azimuthal angle is considered (from 0 to 2π, varying the angle every $\pi/6$, totalling 13 simulations for each Re) following the rotation matrix $\mathfrak{R}_1 = (\alpha, 0)$, while a statistical analysis based on the Weibull statistics is performed to consider the combined effect of azimuthal and polar rotations according to the ordered pair $\mathfrak{R}_2 = (\alpha, \beta)$ with randomly distributed values.

Figure 3(*a*) shows the comparison of the numerical model and the experimental data applied to the smooth sphere, obtained by Achenbach (1972) and fitted by Turton & Levenspiel (1986). The presence and good fitting of the drag crisis is reported at $Re > 3 \times 10^5$. This result allows us to determine the resolution of the mesh, where as Re increases, the size of the cells of the mesh needs to be smaller to capture the turbulent behaviour in the boundary layer and the wake zone. The mesh ratio x/d_p is used, with x being the characteristic length of each mesh element on the particle surface, and the red dashed line in figure 3(*a*) shows the maximum mesh size required to obtain reasonable results, whose percentage difference does not exceed 0.25 %. This translates, for the different simulations, into a range of element numbers from 700 000 (for low Re) to more than 3 000 000 mesh elements (for extremely high Re). Figure 3(*b*) shows the good correlation between the predicted and measured data for the drag coefficient when using this largest mesh size.

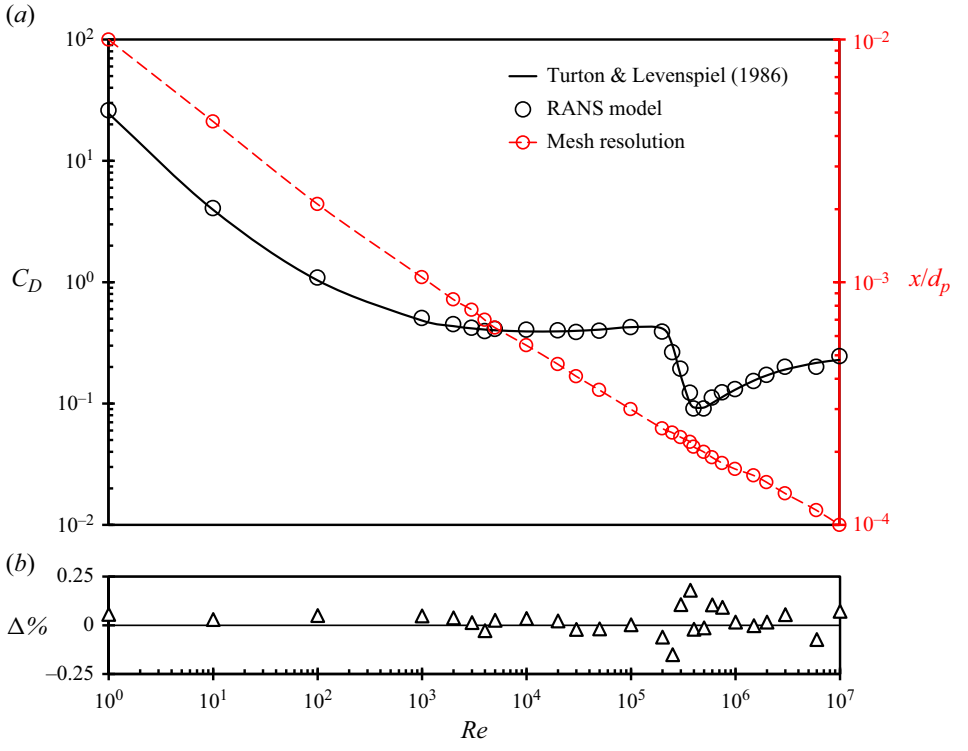

Figure 3. (*a*) Drag coefficient C_D as a function of the Reynolds number *Re* for an isolated smooth sphere. The solid black line represents the fitted experimental values for the smooth sphere (Turton & Levenspiel 1986). The circles represent each numerical simulation. The red dashed line corresponds to the mesh resolution, showing a dependence on *Re*. (*b*) Percentage difference between experimental data and numerical results (in triangles).

The consistency between widely accepted and simulated drag coefficients for spherical grains demonstrated that the RANS model could achieve satisfactory results as long as the mesh refinement in the fluid region is carefully conducted.

3. Results

3.1. *Effect of the Reynolds number*

Figure 4(*a*) shows the drag coefficient C_D as a function of *Re* at different flow incidence angles (azimuthal rotation α) for the LBS and HDG grains. Therein, two extra data points from DNS are also given. They agree well with those from the corresponding RANS simulations. Notably, considering the high number (426) of simulations across seven orders of Reynolds number, it is not possible to run all our simulations using DNS, so we just provide two validation cases for illustrative purposes. In general, the drag coefficient decreases up to values $Re \approx 10\,000$ (subcritical regime). Between these *Re* values and the drag crisis, C_D is independent of the flow regime. Within this zone, the drag coefficient is usually greater than that of the sphere (solid black line in figures 4*a*,*b*) for any incidence angle α, despite having the same decreasing behaviour. This shows the influence of the irregularity of the particle surface, altering the flow conditions inducing irregularities in the streamline patterns. As for smooth spheres, the irregularly shaped particle also suffers a drag crisis with an abrupt decrease of the drag coefficient for values $Re \approx 100\,000$. In fact,

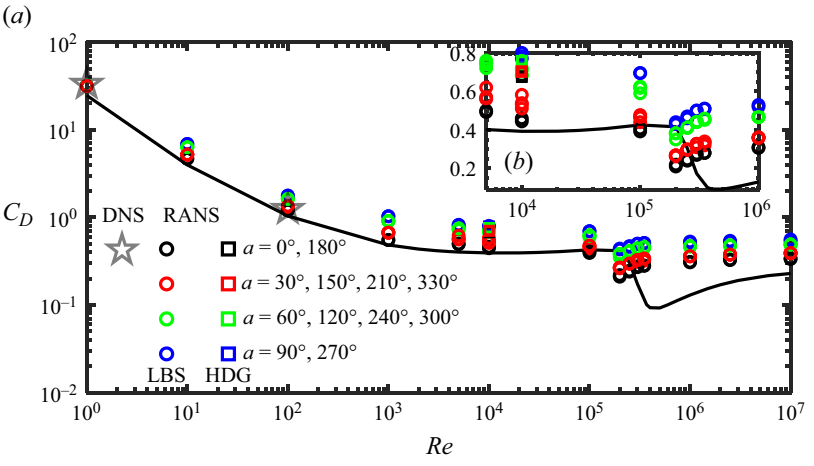

Figure 4. (*a*) Drag coefficient C_D as a function of the Reynolds number Re for the LBS and HDG grains. The black solid line represents the values for the smooth sphere. The markers represent the different simulations performed. The coloured symbols shows the range of values of the azimuthal rotation α. (*b*) Drag coefficient C_D as a function of the Reynolds number Re in the drag crisis.

as is observed for dimpled and rough spheres, the irregularly shaped grain causes a more sudden drop of the drag coefficient, compared to the smooth sphere. This means that the roughness of the surface displaces the boundary layer, causing the drag coefficient to reach its critical value at lower Reynolds numbers ($Re_{cr,sphere} > Re_{cr,grain}$). Figure 4(*b*) presents the drag crisis for the LBS particle, compared to the smooth sphere. It can be observed that the minimum values of the drag coefficient are larger than those of the smooth sphere ($C_D \approx 0.07$). After this crisis, C_D increases again until it is practically independent of the Reynolds number, but dependent on the incidence angle (see the coloured symbols). In summary, a common pattern of the existence of the four flow mechanism zones in terms of C_D arises: (1) subcritical, where C_D decreases as Re increases ($Re < 10^5$); (2) critical, where C_D decreases sharply with growing Re ($10^5 < Re < 2 \times 10^5$); (3) supercritical, beyond the lowest value of C_D, where it increases slightly with increasing turbulence ($2 \times 10^5 < Re < 10^6$); and finally (4) transcritical, where C_D is practically constant at very high values $Re > 10^6$.

3.2. *Effect of the incidence angle*

Figure 5(*a*) represents the behaviour of the drag coefficient as a function of the azimuthal rotation α, for different Reynolds numbers. It clearly shows that as the angle of rotation changes, the drag coefficient increases up to a maximum value. This behaviour reverses as the angle continues to change, repeating itself, similarly to a periodic pattern. This phenomenon is directly associated with the variation of the surface area exposed to the fluid flow. In this case, the minimum projected area coincides with $\alpha = 0$, where the lowest value of the drag coefficient is obtained, repeating the pattern every 180°. Thus as the particle is rotated (increase in α), the drag coefficient increases until it reaches its maximum value when the projected area by the grain is maximum (figures 5*a*,*b*). This is also under the condition that the grain rotation is executed in the same way as was done with the previous studies of drag in ellipsoids, where such a periodic pattern is satisfied. However, this result does not necessarily indicate that two particles with the same

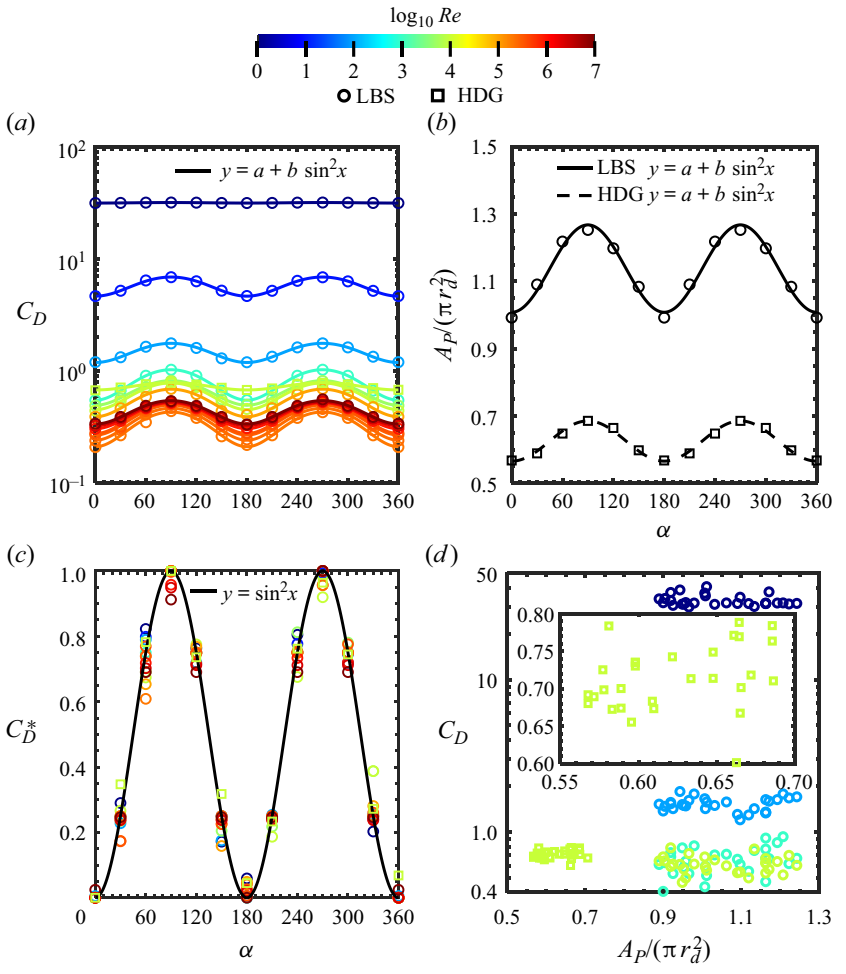

Figure 5. (*a*) Drag coefficient C_D as a function of the angle of incidence of the flow α at different Re for the LBS and HDG grains. (*b*) Normalised projected area $A_P/\pi r_d^2$ as a function of the rotation angle of incidence α (with $\beta = 0$) for both particles. (*c*) Normalised drag coefficient C_D^* as a function of the angle of incidence of the flow α at different Re. The solid line represents the sine-squared function. (*d*) Drag coefficient C_D as a function of the normalised projected area $A_P \pi r_d^2$, at various Reynolds numbers Re. The inset shows these values for HDG grains.

projected area exposed to the flow experience the same drag. Due to the fractal nature of grains, the projected area value on the macro-scale does not necessarily present a π pattern. However, the local characteristics of the fluid flow around the particle present self-affine similarity at the macro-scale, explaining the π-periodicity of the drag coefficient. As can be seen in figure 5(*d*), there is no direct correlation between the drag coefficient and the projected area by the particle. This interesting result is closely related to the fact that a π-periodicity is correlated with the constraint where the flow direction is parallel to the maximum projected area. Sanjeevi & Padding (2017) interpreted the dynamics of this periodic phenomenon in spheroids as an interesting pressure pattern effect imposed by the drag pressure over viscous pressure, especially at high Re.

To better elucidate the rotational dependence, a normalised drag coefficient, defined as $C_D^* \equiv (C_{D,a} - C_{D,min})/(C_{D,max} - C_{D,min})$ is derived to help us to understand the

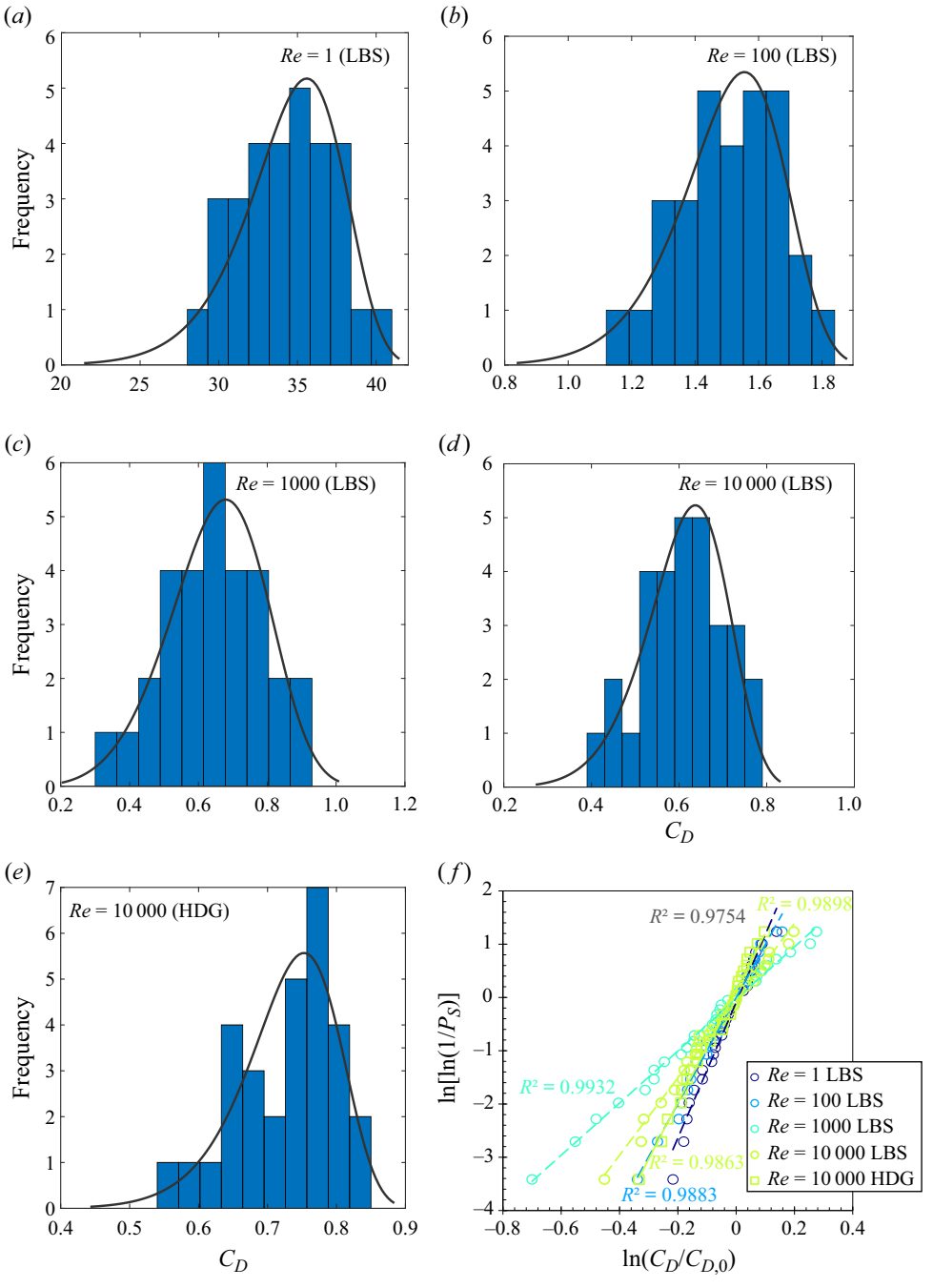

Figure 6. Weibull probability density distributions of the drag coefficient for different random angles of incidence ($\alpha \neq \beta \neq 0$): (*a*) $Re = 1$, (*b*) $Re = 100$, (*c*) $Re = 1000$, (*d*) $Re = 10\,000$, for the LBS grain; (*e*) $Re = 10\,000$ for the HDG grain. (*f*) Plot of $\ln[\ln(1/P_S)]$ versus $\ln(C_D/C_{D,0})$, where P_S is the survival probability distribution.

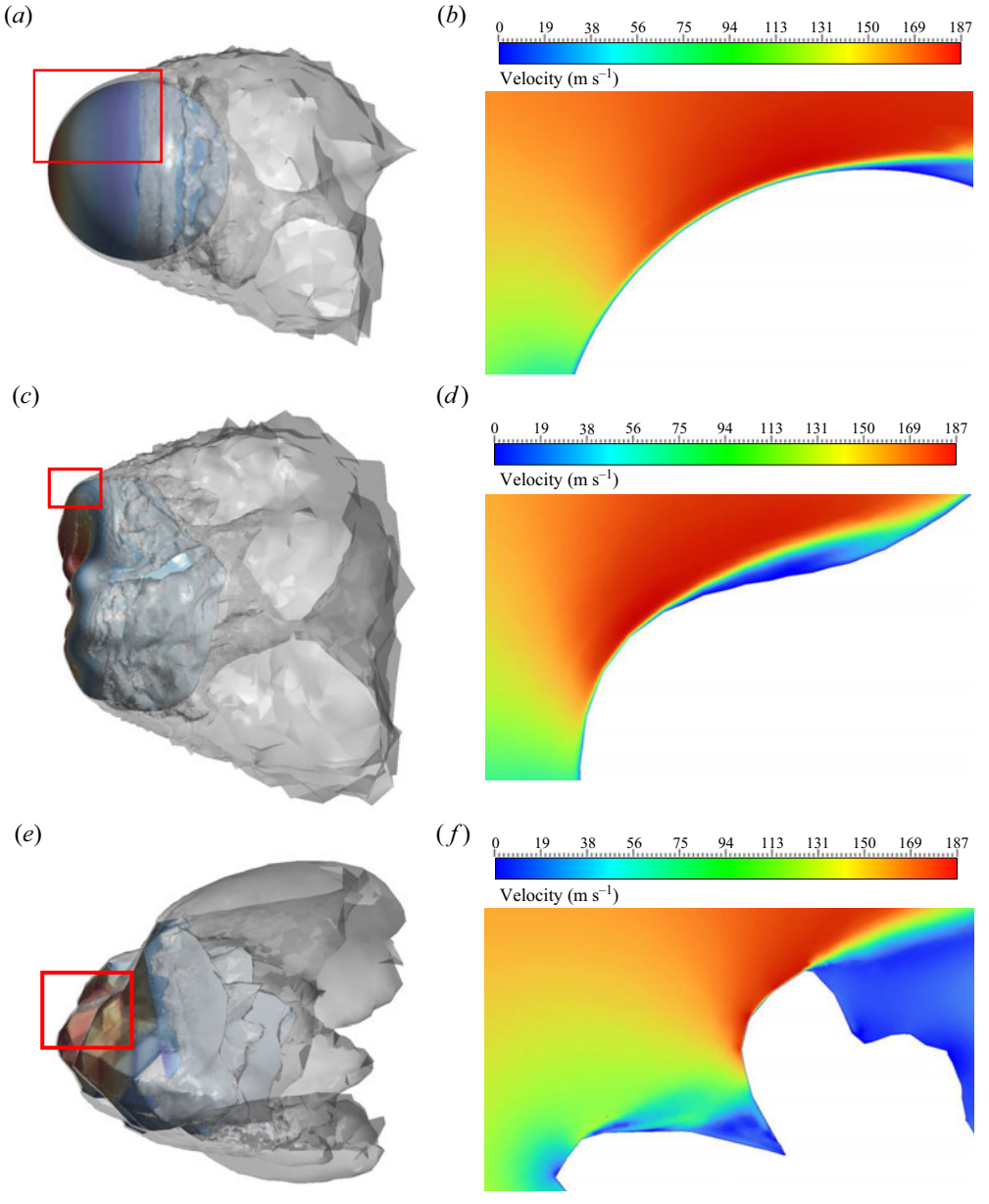

Figure 7. Turbulence patterns of (*a*,*b*) the sphere, (*c*,*d*) the LBS particle, and (*e*,*f*) the HDG particle, for $Re = 100\,000$. Here, (*a*,*c*,*e*) represent the vortex isosurfaces around the sphere and the irregular particles, and (*b*,*d*,*f*) are the velocity fields on a meridional plane.

relationship between the variables. In this case, $C_{D,min}$ is equal to $C_{D,\alpha=0}$, but in general, it would be defined as the minimum value in the plot shown in figure 5(*a*), with another orientation chosen as the initial one. Here, $C_{D,max}$ represents the maximum value. Figure 5(*c*) presents C_D^* as a function of the azimuthal incidence angle α, confirming the cyclic nature, but also, critically almost removing the effect of Re.

In fact, we observe that this normalised drag coefficient is also represented by a sine-squared drag law (3.1) similarly to ellipsoids. This finding allows the understanding

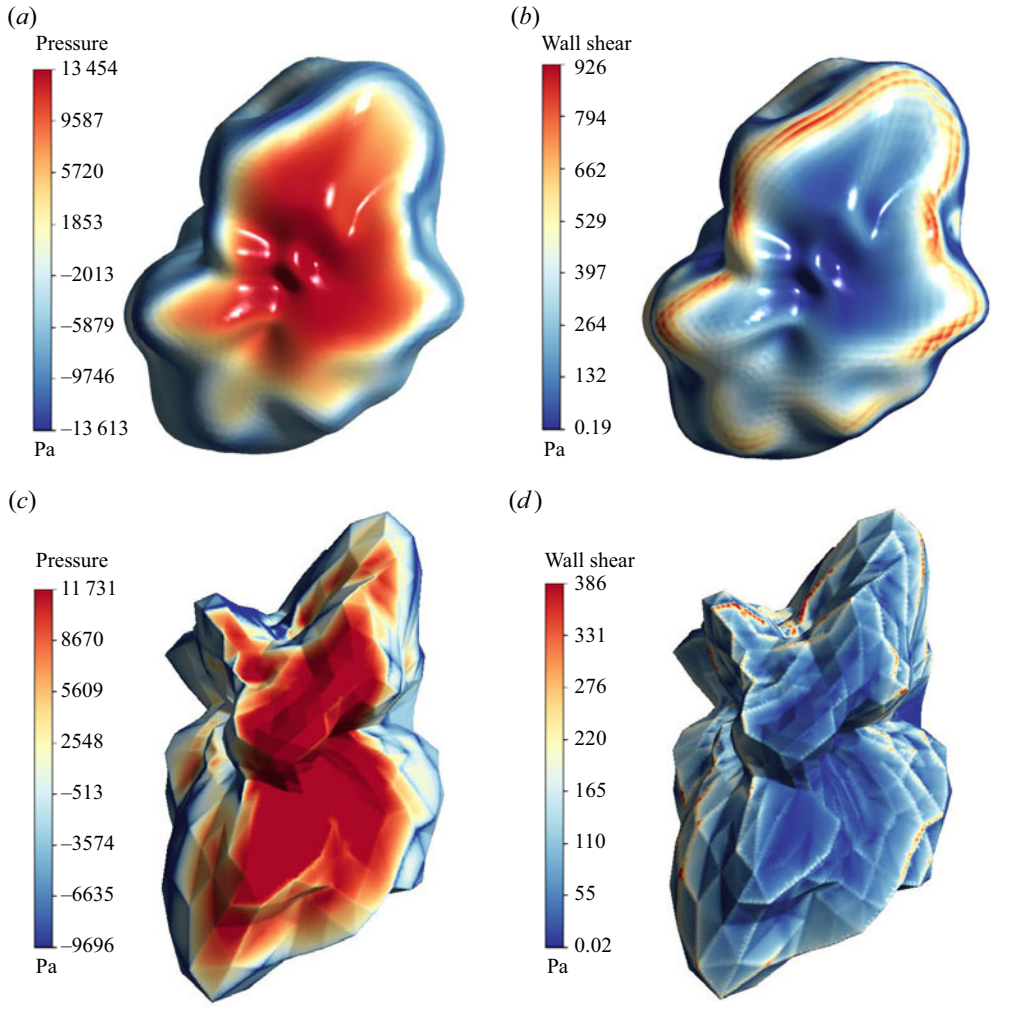

Figure 8. Pressure profiles on the front surface of the flow for (*a*) the LBS particle, and (*c*) the HDG particle. Shear profiles on the front surface of the flow for (*b*) the LBS particle, and (*d*) the HDG particle. The figures correspond to turbulent flow in the critical regime $Re = 100\,000$.

of the hydrodynamics of discrete irregularly shaped particles and facilitates the estimation of the drag coefficient of different geometries based on the orientation of the particle with respect to the fluid flow:

$$C_D = C_{D,min} + (C_{D,max} - C_{D,min}) \sin^2 \alpha. \tag{3.1}$$

A statistical analysis has been developed considering thirty random combination values for both the azimuthal rotation angle α and the polar angle β for both grains. Figures 6(*a–e*) show the distributions of the values of the drag coefficient for four different Reynolds numbers ($Re = 1, 100, 1000, 10\,000$), in both the laminar and turbulent regimes. In the following, we prove that the phenomenon follows a Weibull distribution Weibull (1951).

Hypothesising a Weibullian behaviour of the drag coefficient, we can define its probability density function $PDF(C_D)$ as

$$PDF(C_D) = \frac{m}{\lambda}\left(\frac{C_D}{\lambda}\right)^{m-1} \exp\left[-\left(\frac{C_D}{\lambda}\right)^{m}\right], \quad C_D > 0, \tag{3.2}$$

where C_D is the value of the drag coefficient, and m and λ are the shape and scale parameters of a specific Weibull distribution, respectively. Thus the cumulative distribution function of the drag coefficient $CDF(C_D)$, and the survival probability function $P_s(C_D)$, can be read as

$$CDF(C_D) = 1 - \exp\left[-\left(\frac{C_D}{\lambda}\right)^{m}\right], \quad C_D > 0, \tag{3.3a}$$

$$P_S(C_D) = 1 - CDF(C_D) = \exp\left[-\left(\frac{C_D}{\lambda}\right)^{m}\right], \quad C_D > 0, \tag{3.3b}$$

where λ could be approximated by a characteristic drag coefficient $C_{D,0}$ with $P_S(C_{D,0}) \approx 37\,\%$. Finally, (3.3*b*) can be described in logarithmic terms as

$$\ln[\ln(1/P_S)] = m\ln(C_D) - m\ln(C_{D,0}). \tag{3.4}$$

From (3.4), it is possible to find the parameters of the Weibull modulus m as shown in figure 6(*f*). The large R^2 (> 0.975) values show the fidelity of the Weibullian behaviour.

3.3. *Boundary layer separation and turbulence*

One of the characteristics of external flows is the existence of a thin layer between the solid body and the fluid. This boundary layer varies depending on the flow regime and the surface of the solid body. In the case of smooth spheres, it is well studied that boundary layer separation occurs at approximately 80° (relative to flow direction) in the subcritical regime (prior to drag crisis), and 120° in the supercritical regime (Achenbach 1972). However, in irregularly shaped particles, more than one separation point is possible, and there is ambiguity in defining the separation line, so we restrict ourselves here to show its existence in the turbulent regime. In figure 7, we present the turbulence patterns in the critical regime, at $Re = 100\,000$. The influence of the irregularity of the particle surface in the separation of the boundary layer can be observed, where defining its geometry precisely is complex, considering the flow patterns in it. Thus in figures 7(*a*,*c*,*e*), the pattern of the vorticity isosurfaces is shown, where its increase occurs mainly at the poles of the particle, giving rise to the separation of the boundary layer. Figures 7(*b*,*d*,*f*) represent the velocity field contours, highlighting the formation of turbulence and the chaotic pattern behind the particle. It is important to discuss that due to the irregularity of the particle surface, there may be an artificial separation of the boundary layer when the surface is not smooth, despite the fact that it is irregular on a larger scale. In figure 7(*f*), it can be seen that there is more than one boundary layer separation at small scale, characterised by zones of low to zero velocity, which reflects the difficulty of quantifying the effect of turbulence on the global dynamic behaviour of the particle.

Figures 8(*a*,*c*) show the pressure patterns at $Re = 100\,000$. The high-pressure points are concentrated on the front face that is normal to the flow, impacting the grain directly on the entire perpendicular area exposed to the fluid. Figures 8(*b*,*d*) show the shear stresses for the same regime for both irregularly shaped grains. Here, the points that experience

the most shear coincide with the points of least pressure. This phenomenon occurs due to the characteristics of the boundary layer, which allows the flow lines to be displaced by 'dragging' the fluid around the particle surface.

4. Conclusions

The drag coefficient C_D of irregularly shaped particles in a wide range of Re and flow incidence angles was studied. At high Re, we show the existence of the drag crisis for this type of geometry, a well-described and understood phenomenon for bodies of simple geometry. However, for both geometries it is shown that Re_c is lower than that for the sphere, accelerating this crisis. The angle of incidence shows a periodic behaviour of the drag coefficient with respect to the azimuthal angle of incidence of the flow, and fits to a sine-squared function. This also occurs even at very high Reynolds numbers (turbulence regime), thus extending the model described previously for spheroids, ellipsoids and smooth shapes within the laminar regime. The value of the drag coefficient can therefore be estimated for any angle of rotation (around the same axis) knowing only two values – in this case, a minimum value and a maximum value – using the suggested normalised definition of the drag coefficient C_D^*. The separation of the boundary layer in irregular bodies is characterised by flow patterns that are not well defined due to the irregularity of the particle surface, but which rely directly on the regularity of the surface in front of the flow, inducing the formation of vortices and eddies past flow depending on the degree of separation of the boundary layer.

Finally, the orientational dependence of the drag coefficient satisfies the Weibull behaviour, caused by both the randomness of the rotation and the position of the particle in the flow.

With this, we hope to inject interest in the study of the hydrodynamic behaviour of irregularly shaped particles, to extend its knowledge and encourage the analysis of highly turbulent flows around irregular bodies. This will also be useful to endless applications in geosciences and different disciplines of engineering.

Funding. This work is part of the support granted by the National Scientific Research Agency of Chile – Grant for Doctoral Studies no. 62210003 for Á.V., and by the Australian Research Council (ARC) – the Discovery Early Career Award (DECRA) no. DE240101106 for D.W. The corresponding author D.W. thanks Alexander von Humboldt Foundation for providing the Humboldt Fellowship hosted in RWTH Aachen. The authors thanks Professor C. Zhai in Xi'an Jiaotong University, China, for providing the ANSYS® Fluent® licence and computational resources via the Open Research Funding no. SV2021-KF-28. Associate Professor Y. Gan is thanked for the inspired and fruitful discussions of this study.

Declaration of interests. The authors report no conflict of interest.

Authorship and contributorship. Á.V.: Data curation, Investigation, Methodology, Visualization, Writing – original draft, and Writing – review & editing. D.W.: Conceptualization, Data curation, Formal analysis, Funding acquisition, Investigation, Methodology, Project administration, Resources, Software, Supervision, Validation, Visualization, and Writing – review & editing. R.F.: Writing – review & editing.

Author ORCIDs.
Álvaro Vergara https://orcid.org/0009-0003-4257-1442;
Deheng Wei https://orcid.org/0000-0002-1787-6389.

References

ACHENBACH, E. 1972 Experiments on the flow past spheres at very high Reynolds numbers. *J. Fluid Mech.* **54**, 565–575.

ANGELIDAKIS, V., NADIMI, S. & UTILI, S. 2022 Elongation, flatness and compactness indices to characterise particle form. *Powder Technol.* **396**, 689–695.

BAYINDIRLI, C. & ÇELIK, M. 2018 The experimentally and numerically determination of the drag coefficient of a bus model. *Intl J. Automot. Engng Technol.* **3**, 117–123.

BERATLIS, N., BALARAS, E. & SQUIRES, K. 2019 On the origin of the drag force on dimpled spheres. *J. Fluid Mech.* **879**, 147–167.

CADOT, O., DESAI, A., MITTAL, S., SAXENA, S. & CHANDRA, B. 2015 Statistics and dynamics of the boundary layer reattachments during the drag crisis transitions of a circular cylinder. *Phys. Fluids* **27**, 1–24.

CHEN, S., CHEN, P. & FU, J. 2022 Drag and lift forces acting on linear and irregular agglomerates formed by spherical particles. *Phys. Fluids* **34**, 1–15.

CONSTANTINESCU, G. & SQUIRES, K. 2004 Numerical investigations of flow over a sphere in the subcritical and supercritical regimes. *Phys. Fluids* **16**, 1449–1466.

DEFRAEYE, T., VERBOVEN, P. & NICOLAI, B. 2013 CFD modelling of flow and scalar exchange of spherical food products: turbulence and boundary-layer modelling. *J. Food Engng* **114**, 495–504.

DIOGUARDI, F., MELE, D. & DELLINO, P. 2017 A new one-equation model of fluid drag for irregularly shaped particles valid over a wide range of Reynolds numbers. *J. Geophys. Res.: Solid Earth* **123**, 1–13.

ETMINAN, V., LOWE, R. & GHISALBERTI, M. 2017 A new model for predicting the drag exerted by vegetation canopies. *Water Resour. Res.* **53**, 3179–3196.

GAI, G. & WACHS, A. 2023 High fidelity adaptive Cartesian octree grid computations of the flow past a Platonic polyhedron up to a Reynolds number of 200. *Powder Technol.* **420**, 1–20.

GUILLARD, F., FORTERRE, Y. & POULIQUEN, O. 2014 Lift forces in granular media. *Phys. Fluids* **26**, 1–16.

HAIDER, A. 1989 Drag coefficient and terminal velocity of spherical and nonspherical particles. *Powder Technol.* **58**, 63.

JING, L., OTTINO, J., UMBANHOWAR, P. & LUEPTOW, R. 2022 Drag force in granular shear flows: regimes, scaling laws and implications for segregation. *J. Fluid Mech.* **948**, 1–27.

LAM, K. & LIN, Y.F. 2009 Effects of wavelength and amplitude of a wavy cylinder in cross-flow at low Reynolds numbers. *J. Fluid Mech.* **620**, 195–220.

MENTER, F.R. 1994 Two-equation eddy-viscosity turbulence models for engineering applications. *AIAA J.* **32**, 1598–1605.

MICHAELIDES, E. & FENG, Z. 2023 Review – drag coefficients of non-spherical and irregularly-shaped particles. *Trans. ASME J. Fluids Engng* **145**, 1–20.

OGGIANO, L., SAETRAN, L., LØSET, S. & WINTHER, R. 2004 Reducing the athlete's aerodynamical resistance. *J. Appl. Comput. Mech.* **8** (2).

OUCHENE, R., KHALIJ, M., TANIÈRE, A. & ARCEN, B. 2015 Drag, lift and torque coefficients for ellipsoidal particles: from low to moderate particle Reynolds numbers. *Comput. Fluids* **113**, 53–64.

ROY, C., PAYNE, J., MCWHERTER-PAYNE, M. & SALARI, K. 2006 RANS simulations of a simplified tractor/trailer geometry. *Trans. ASME J. Fluids Engng* **128**, 1083–1089.

SANJEEVI, S., KUIPERS, J. & PADDING, J. 2018 Drag, lift and torque correlations for non-spherical particles from Stokes limit to high Reynolds numbers. *Intl J. Multiphase Flow* **106**, 325–337.

SANJEEVI, S. & PADDING, J. 2017 On the orientational dependence of drag experienced by spheroids. *J. Fluid Mech.* **820**, 1–13.

SOMMERFELD, M. & QADIR, Z. 2018 Fluid dynamic forces acting on irregular shaped particles: simulations by the Lattice-Boltzmann method. *Intl J. Multiphase Flow* **101**, 212–222.

SUN, M., SAITO, T., TAKAYAMA, K. & TANNO, H. 2005 Unsteady drag on a sphere by shock wave loading. *Shock Waves* **14**, 3–9.

SUN, Q., ZHAO, G., PENG, W., WANG, J., JIANG, Y. & YU, S. 2018 Numerical predictions of the drag coefficients of irregular particles in an HTGR. *Ann. Nucl. Energy* **115**, 195–208.

TRAN-CONG, S., GAY, M. & MICHAELIDES, E. 2004 Drag coefficients of irregularly shaped particles. *Powder Technol.* **139**, 21–32.

TSUKROV, I., DRACH, A., DECEW, J., SWIFT, M.R. & CELIKKOL, B. 2011 Characterization of geometry and normal drag coefficients of copper nets. *Ocean Engng* **38**, 1979–1988.

TURTON, R. & LEVENSPIEL, O. 1986 A short note on the drag correlation for spheres. *Powder Technol.* **47**, 83–86.

WANG, Y., ZHOU, L., WU, Y. & YANG, Q. 2018 New simple correlation formula for the drag coefficient of calcareous sand particles of highly irregular shape. *Powder Technol.* **326**, 379–392.

WEI, D., WANG, J., NIE, J. & ZHOU, B. 2018 Generation of realistic sand particles with fractal nature using an improved spherical harmonic analysis. *Comput. Geotech.* **104**, 1–12.

WEIBULL, W. 1951 A statistical distribution function of wide applicability. *J. Appl. Mech.* **18**, 290–293.

YANG, X., GUPTA, S., KUO, T. & GOPALAKRISHNAN, V. 2014 RANS and large eddy simulation of internal combustion engine flows – a comparative study. *Trans. ASME J. Engng Gas Turbines Power* **136**, 1–9.

ZHANG, F., HE, Y., XIE, W., WEI, N., LI, J., WANG, S. & WANG, J. 2023 Drag coefficients for elongated/flattened irregular particles based on particle-resolved direct numerical simulation. *Powder Technol.* **418**, 1–30.